Facile Synthesis of Pd–Pt Alloy Nanocages and Their Enhanced Performance for Preferential Oxidation of CO in Excess Hydrogen

Hui Zhang,[†,‡,#] Mingshang Jin,[†,§,#] Hongyang Liu,[∥] Jinguo Wang,[⊥] Moon J. Kim,[⊥] Deren Yang,[‡] Zhaoxiong Xie,[§] Jingyue Liu,[∥] and Younan Xia[†,*]

[†]Department of Biomedical Engineering, Washington University, St. Louis, Missouri 63130, United States, [‡]State Key Laboratory of Silicon Materials and Department of Materials Science and Engineering, Zhejiang University, Hangzhou, Zhejiang 310027, People's Republic of China, [§]State Key Laboratory for Physical Chemistry of Solid Surfaces and Department of Chemistry, Xiamen University, Xiamen, Fujian 361005, People's Republic of China, [⊥]Department of Materials Science, University of Texas at Dallas, Richardson, Texas 75083, United States, and [∥]Center for Nanoscience, Department of Physics and Astronomy, and Department of Chemistry and Biochemistry, University of Missouri-St. Louis, St. Louis, Missouri 63121, United States. [#]These two authors contributed equally to this work.

ABSTRACT This article describes a new method for the facile synthesis of Pd–Pt alloy nanocages with hollow interiors and porous walls by using Pd nanocubes as sacrificial templates. Differing from our previous work (Zhang, H.; Jin, M. S.; Wang, J. G.; Li, W. Y.; Camargo, P. H. C.; Kim, M. J.; Yang, D. R.; Xie, Z. X.; Xia, Y. Synthesis of Pd-Pt Bimetallic Nanocrystals with a Concave Structure through a Bromide-Induced Galvanic Replacement Reaction. *J. Am. Chem. Soc.* 2011, *133*, 6078–6079), we complemented the galvanic replacement (between Pd nanocubes and $PtCl_4^{2-}$) with a coreduction process (for $PdCl_4^{2-}$ from the galvanic reaction and $PtCl_4^{2-}$ from the feeding) to generate Pd–Pt alloy nanocages in one step. We found that the rate of galvanic replacement (as determined by the concentrations of Br^- and $PtCl_4^{2-}$ and temperature) and the rates of coreduction (as determined by the type of reductant and temperature) played important roles in controlling the morphology of resultant Pd–Pt alloy nanocages. The Pd–Pt nanocages exhibited both enhanced activity and selectivity for the preferential oxidation (PROX) of CO in excess hydrogen than those of Pd nanocubes and the commercial Pt/C thanks to the alloy composition and hollow structure. In addition, as the sizes of the Pd–Pt nanocages decreased, they exhibited higher CO conversion rates and lower maximum conversion temperatures due to the increase in specific surface area.

KEYWORDS: Pd–Pt alloy nanocages · PROX · galvanic replacement · coreduction · Pd nanocubes

Proton-exchange membrane fuel cells (PEMFCs), which efficiently convert the chemical energy of hydrogen into electricity with only water as a byproduct, possess great potential as substitutes for conventional combustion engines in future mobile applications due to their high energy-efficiency and essentially no emission of pollutants.[1–5] As the workhorse of many industrial catalysts, Pt is also a critical component of the PEMFC technology, where it acts as the most effective catalyst for the oxygen reduction reaction (ORR) and fuel (e.g., hydrogen) oxidation reaction.[6–10] Unfortunately, Pt-based anodes are vulnerable to the poisoning effect associated with the residual CO in a H_2 stream during the hydrogen oxidation reaction.[11–14] As such, delivery of pure hydrogen to the Pt-based anodes becomes a necessary requirement for the practical operation of PEMFCs, and preferential oxidation (PROX) of CO in the presence of excess hydrogen thus becomes a key process for the production of pure hydrogen fuel.[15–17] Recently, considerable research has been devoted to the search of a solution to the CO poisoning problem by combining Pt with other metals to increase the oxidation rate of CO, thus lowering the maximum conversion temperature.[18–20] Among various metals, Pd has been identified as a promising candidate for formulating Pd–Pt bimetallic catalysts with an alloy or core–shell structure for the PROX reaction due to its relatively low cost (only one-third of that of Pt), excellent catalytic activity, and CO tolerance.[21–23]

Enhancing the catalytic performance also requires the use of Pt in a finely divided state. For this reason, many efforts have been directed to the production of Pt-based nanostructures with uniform sizes and well-defined morphologies.[24–28] In particular, Pt-based nanoparticles with hollow interiors are of great interest and importance for catalytic and electrocatalytic applications as they can provide higher specific surface areas and thus improved activities as compared to their solid counterparts.[29,30] The presence of a cavity in the interior can also help further reduce the loading of Pt, an

* Address correspondence to xia@biomed.wustl.edu.

Received for review July 30, 2011 and accepted September 3, 2011.

Published online September 03, 2011
10.1021/nn202896q

extremely rare and expensive noble metal.[31,32] In general, nanoparticles with hollow interiors are commonly prepared by coating the surface of colloidal particles with thin layers of the desired materials (or its precursor), followed by selective removal of the colloidal templates through calcination or wet chemical etching.[33,34] However, metal nanoparticles with hollow interiors prepared using this method were often troubled by limitations such as rough surfaces, polycrystallinity, nonuniformity in shell thickness, poorly defined composition, and difficulty in removing the colloidal templates without breaking the shells.[35,36] Recently, our group has developed a facile and versatile method based on the galvanic replacement reaction for generating noble-metal nanoparticles with hollow interiors and/or porous walls or more specifically in the formation of nanocages or nanoboxes using Ag nanocubes as sacrificial templates.[37,38] The size and morphology of the final product can be readily manipulated by using sacrificial templates with different sizes and shapes and/or by controlling the extent of replacement. Most recently, we also demonstrated the feasibility to achieve galvanic replacement between H_2PtCl_6 and Pd nanocrystals in the presence of KBr.[39] Different from the system involving Ag templates, the galvanic replacement between Pd nanocrystals and $PtCl_6^{2-}$ ions was preferentially initiated and continued on the {100} facets of Pd nanocrystals while the resultant Pt atoms were mainly deposited on the corners, resulting in the formation of Pd–Pt bimetallic concave nanocrystals instead of nanocages.[39] To generate Pd–Pt alloy nanocages with hollow interiors and porous walls, here we introduce a codeposition process for the Pd and Pt atoms in addition to the galvanic replacement, with the introduction of citric acid (CA) as a reducing agent for both the Pd and Pt salt precursors.

The synthesis was typically conducted in a mixture containing Pd nanocubes and K_2PtCl_4 in the presence of KBr, with CA as a reducing agent. The success of this synthesis relies on an interplay of two different reactions: (i) the galvanic replacement between Pd nanocubes and $PtCl_4^{2-}$ ions and (ii) the coreduction of $PdCl_4^{2-}$ derived from the galvanic replacement and $PtCl_4^{2-}$ added into the system. In the initial stage, Pd atoms were preferentially oxidized and dissolved from the {100} facets of Pd nanocubes by reacting with $PtBr_4^{2-}$ *via* a galvanic replacement mechanism. As the galvanic reaction proceeded, the Pd nanocube gradually disappeared, accompanied by the formation of a Pd–Pt concave nanocube. Meanwhile, the Pd^{2+} ions derived from the galvanic replacement, together with the $PtCl_4^{2-}$ ions remaining in the solution, were coreduced into atoms by CA and then deposited on the side faces of the concave nanocube. Because of the formation of an alloy with Pt, the newly formed Pd in the walls was less vulnerable to galvanic replacement than the pure Pd in the original nanocube. As such, a Pd–Pt alloy nanocage with a cubic morphology was formed *via* a combination of Pd dissolution (due to galvanic replacement) and Pd–Pt overgrowth (due to coreduction). The Pd–Pt alloy nanocages with hollow interiors and porous walls were then evaluated as catalysts for PROX. Our data clearly demonstrate that the Pd–Pt alloy nanocages had substantially enhanced CO conversion and selectivity at low temperatures as compared with Pd nanocubes and the commercial Pt/C catalyst.

RESULTS AND DISCUSSION

For the standard synthesis of Pd–Pt alloy nanocages, Pd nanocubes of 18 nm in average edge length (Figure S1A,B in the Supporting Information) were employed as sacrificial templates. A close examination shows that some of the Pd nanocubes might have a slightly elongated morphology, with their surfaces being still covered by {100} facets. For the purpose of simplicity, we collectively call them "nanocubes" in the present work. Figure 1 shows scanning electron microscopy (SEM), high angle annular dark field scanning transmission electron microscopy (HAADF-STEM), energy dispersive X-ray (EDX), and high-resolution transmission electron microscopy (HRTEM) images of the Pd–Pt alloy nanocages prepared using the standard procedure. The SEM image in Figure 1A indicates that most of the Pd–Pt nanocages still had a cubic shape, with a slightly larger size than that of the original Pd cubes. In addition, the Pd–Pt nanocages exhibited a darker contrast in the center relative to the edges (inset of Figure 1A), implying the formation of a hollow structure in the interior. The hollow structure was also supported by the HAADF-STEM image in Figure 1B. Moreover, there are a large number of pores on the surface of each nanocage, which might be of great significance to catalytic applications as the pores will increase the specific surface area and allow for the transport of reagents/products. The elemental distribution of Pd and Pt in the nanocage was measured by both EDX mapping and line-scan analysis. Figure S2 in the Supporting Information shows an EDX spectrum taken from the Pd–Pt nanocages. It shows five major elements in the sample: Pd, Pt, Br, C, and Cu. Obviously, Pd and Pt came from the Pd–Pt nanocages while Br, C, and Cu originated from the reactants (KBr and PVP) and the carbon-coated Cu grid, respectively. The elemental mapping in Figure 1C revealed that the nanocage was made of an alloy, with both Pd and Pt homogeneously distributed throughout the nanocage. The Pd–Pt alloy structure was also supported by the data of EDX line-scan (Figure 1C) recorded through the middle plane of a single nanocage. As observed, both Pd and Pt traces have two peaks at the edges and one valley in the center. The positions of peaks and valley for the

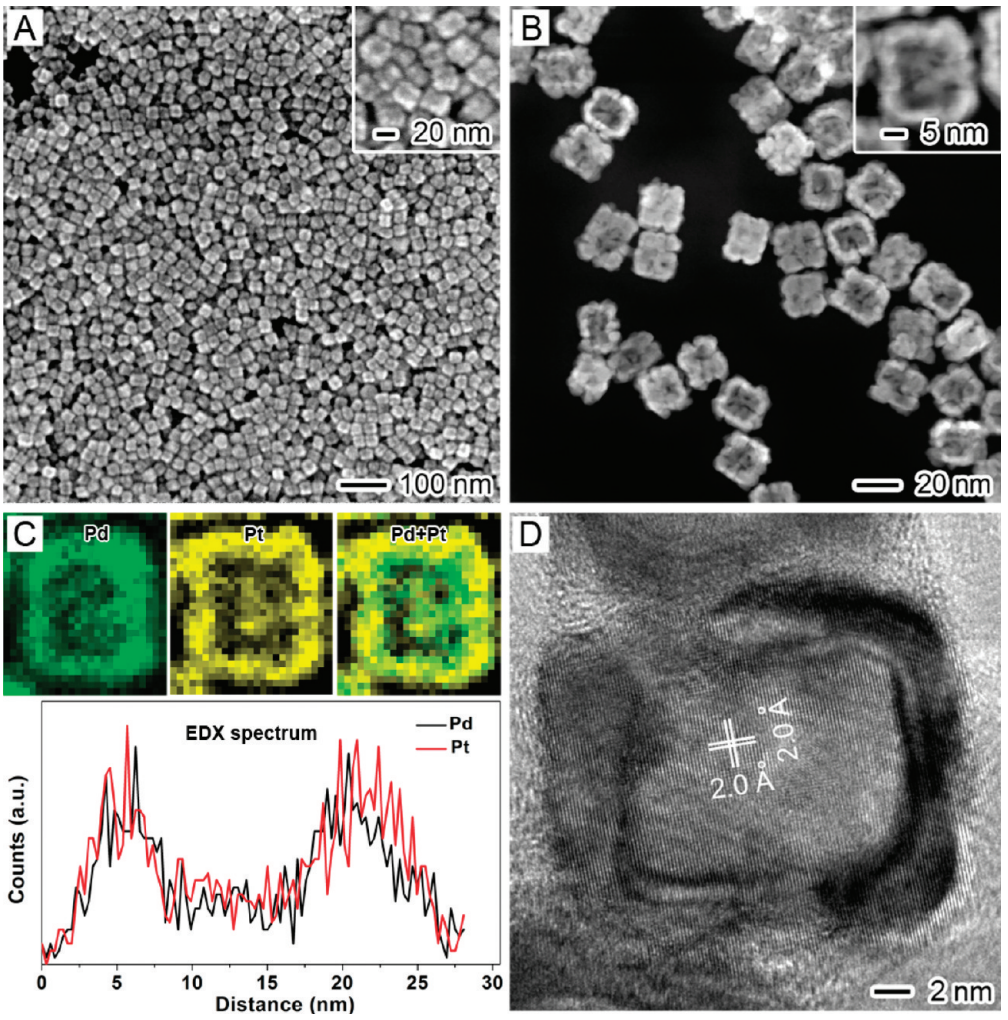

Figure 1. Characterizations of morphology, structure, and composition of the Pd–Pt alloy nanocages prepared using the standard procedure. (A) SEM image, (B) HADDF-STEM image, (C) EDX mapping and line-scan profile, and (D) HRTEM image. The insets in parts A and B show the images of the nanocrystals at a higher magnification. The green and yellow colors in part C correspond to Pd and Pt elements, respectively.

Pd trace matches well with those for the Pt trace, confirming an alloy structure. Figure 1D shows a typical HRTEM image of an individual Pd–Pt nanocage along the [100] zone axis. This image clearly shows well-resolved, continuous fringes in the same orientation, indicating that the nanocage was a single crystal. We believe that the same crystal structure and negligible lattice mismatch between Pd and Pt (0.77%) were responsible for the formation of a single-crystal, Pd–Pt alloy nanocage *via* a combination of galvanic replacement and codeposition. The fringes with lattice spacing of 2.0 Å can be indexed to the {200} planes of a face-centered cubic (*fcc*) lattice, indicating that the side face of the nanocages is likely bounded by {100} facets.

In order to decipher the formation mechanism of the Pd–Pt alloy nanocages, a series of TEM images were taken from the samples prepared at different reaction times, as shown in Figure 2. In the initial stage (Figure 2A, t = 0.5 h), the side faces of Pd nanocubes were slightly concaved, which can be attributed to the bromide-induced galvanic replacement.[39] When the reaction was extended to t = 2 h (Figure 2B), however, the concave regions on the surface of Pd nanocube were gradually filled due to the accompanying codeposition of Pd and Pt, and this differs completely from our previous observation during the synthesis of Pd–Pt concave nanocrystals.[39] The magnified TEM image (inst of Figure 2B) shows that a number of pores were formed on the surface of resultant Pd–Pt nanocrystals due to the continuation of galvanic replacement. After the reaction had proceeded to t = 6 h (Figure 2C), essentially all the Pd nanocubes had been transformed into Pd–Pt nanocages with hollow interiors. According to the standard procedure, a reaction time of 12 h was sufficient to generate Pd–Pt nanocages in high quality. Further extension of the time to 15 h (Figure 2D) did not result in any change in size and morphology for the nanocages. Taken together, it is clear that the formation of Pd–Pt

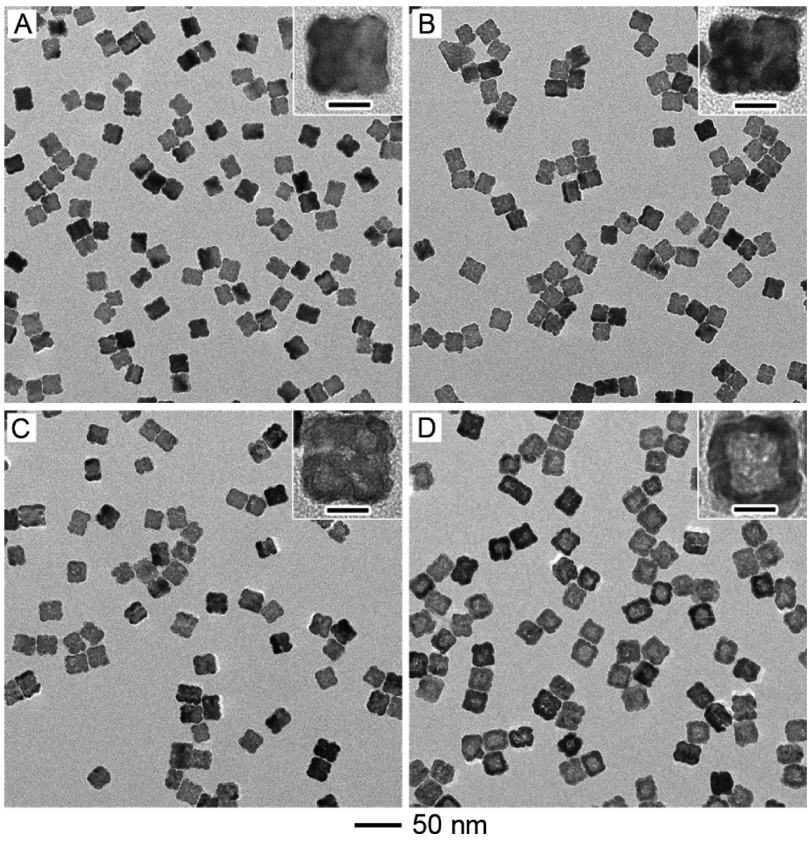

Figure 2. TEM images of Pd−Pt alloy nanostructures obtained using the standard procedure, except for different periods of time: (A) 0.5, (B) 2, (C) 6, and (D) 15 h. The insets show TEM images of individual nanocrystals at a higher magnification. The scale bars in the insets are 10 nm.

nanocages involves a morphological transition from solid nanocubes to concave nanocubes and then nanocages with hollow interiors and porous walls through a combination of galvanic replacement and coreduction.

We have also systematically evaluated the effects of various parameters on the synthesis, including the amount of K_2PtCl_4, the temperature, the type of reducing agent, and the presence or absence of KBr. Figure 3 shows TEM images of Pd−Pt alloy nanocrystals that were formed *via* a combination of galvanic replacement between Pd nanocubes and different amounts of K_2PtCl_4 and codeposition of the Pd and Pt atoms formed due to reduction by CA. When 0.7 mg of K_2PtCl_4 was added (Figure 3A), the side faces of Pd nanocubes were excavated due to bromide-induced galvanic replacement, leading to the formation of concave nanocubes (see the inset of Figure 3A). Because of the insufficient supply of K_2PtCl_4, galvanic replacement instead of codeposition prevailed in this case. When reacted with 2.8 mg of K_2PtCl_4 (Figure 3B), all the side faces were further etched due to galvanic replacement. The magnified TEM image (inset of Figure 3B) shows that a small hollow interior in the center of a concave nanocube was formed due to the continuous dissolution of Pd atoms *via* galvanic replacement. On the other hand, the Pd^{2+} ions coming from the galvanic replacement and the remaining $PtCl_4^{2-}$ ions were coreduced by CA. The newly formed Pd and Pt atoms were deposited on the side faces of a nanocube, resulting in the formation of enlarged bumps at the tips together with a decrease in concave volume. When the amount of K_2PtCl_4 was increased to 7 mg (Figure 3C), the hollow interiors of the Pd−Pt nanocrystals were gradually enlarged due to galvanic replacement. The magnified TEM image (inset of Figure 3C) indicates that the newly formed Pd and Pt atoms were preferentially added to the concave regions on the side faces, leading to the formation of Pd−Pt alloy nanocages with a cubic shape. As the amount of K_2PtCl_4 was further increased to 28 mg (Figure 3D), high-quality Pd−Pt alloy nanocages with an average edge length of 20 nm were obtained. A careful analysis (inset of Figure 3D) shows that there were a number of small pores on the walls of the nanocage. These pores could serve as channels for ion transportation during galvanic replacement, and they played an important role in the formation of high-quality Pd−Pt alloy nanocages. Further increasing the amount of K_2PtCl_4 to 70 mg (Figure S3A,B in the Supporting Information) resulted in excess deposition of Pt on the Pd−Pt nanocages, generating a rough surface. It should be pointed out that not only the shape of Pd−Pt nanocrystals evolved from cube to

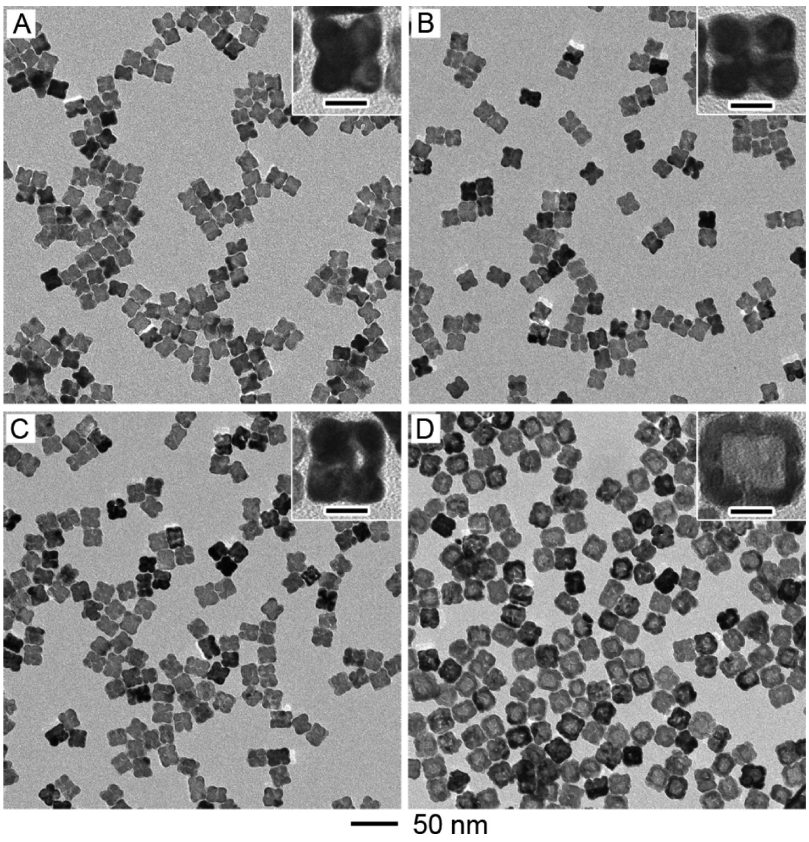

Figure 3. TEM images of Pd−Pt alloy nanostructures obtained using the standard procedure, except for the addition of different amounts of K_2PtCl_4: (A) 0.7, (B) 2.8, (C) 7, and (D) 28 mg. The insets show TEM images of individual nanocrystals at a higher magnification. The scale bars in the insets are 10 nm.

cage during the reaction, their composition also changed according to the data from inductively coupled plasma-mass spectrometry (ICP-MS) analysis. When 0.7 mg of K_2PtCl_4 was added, the molar ratio of Pt to Pd in the final product was 1:6. This ratio was also increased with increasing the amount of K_2PtCl_4. For example, supply of K_2PtCl_4 in the amounts of 2.8, 7.0, and 28.0 mg would result in Pt to Pd molar ratios of roughly 1:3, 1:2, and 2:1, respectively.

The reaction temperature was also found to play an important role in the formation of Pd−Pt alloy nanocages since the rates of galvanic replacement and reduction were strongly dependent on this parameter. Figure S4 in the Supporting Information shows TEM images of Pd−Pt nanocrystals that were obtained using the standard procedure except for the difference in reaction temperature. When the reaction was conducted at 50 °C (Figure S4A in the Supporting Information) or 60 °C (Figure S4B in the Supporting Information), the Pd nanocubes were slightly excavated at the side faces due to galvanic replacement, resulting in the formation of Pd−Pt concave nanocubes. However, the rate of galvanic replacement was so slow at these two temperatures that the supply of Pd^{2+} ions was insufficient and no obvious codeposition of Pd and Pt was observed. At 70 °C (Figure S4C in the Supporting Information), the concave region was gradually filled due to codeposition of Pd and Pt, together with a large number of small pores on the surface of the nanocrystals. As the temperature was further increased to 80 °C (Figure S4D in the Supporting Information), a small hollow interior started to appear in the center of the Pd−Pt nanocrystal. High-quality Pd−Pt nanocages could not be obtained unless the reaction was conducted at 90 °C. In general, the use of an elevated temperature could speed up the galvanic replacement between Pd nanocubes and $PtCl_4^{2-}$ ions as well as the codeposition of Pd and Pt atoms; both of them are beneficial to the formation of Pd−Pt alloy nanocages with hollow interiors.

Figure S5A in the Supporting Information shows a TEM image of Pd−Pt nanocrystals prepared using the standard procedure except for the absence of CA. As can be seen, Pd−Pt nanocrystals with small hollow interiors were obtained, which could be attributed to the galvanic replacement and codeposition of Pd and Pt atoms due to reduction by PVP.[40] However, careful analysis (inset of Figure S5A in the Supporting Information) shows that the side faces of the Pd−Pt nanocrystals were still concave due to the weaker reducing power of PVP than that of CA. When AA was used as a reducing agent (Figure S5B in the Supporting Information), $PtCl_4^{2-}$ ions were preferentially reduced by AA instead of galvanic replacement, leading to the formation

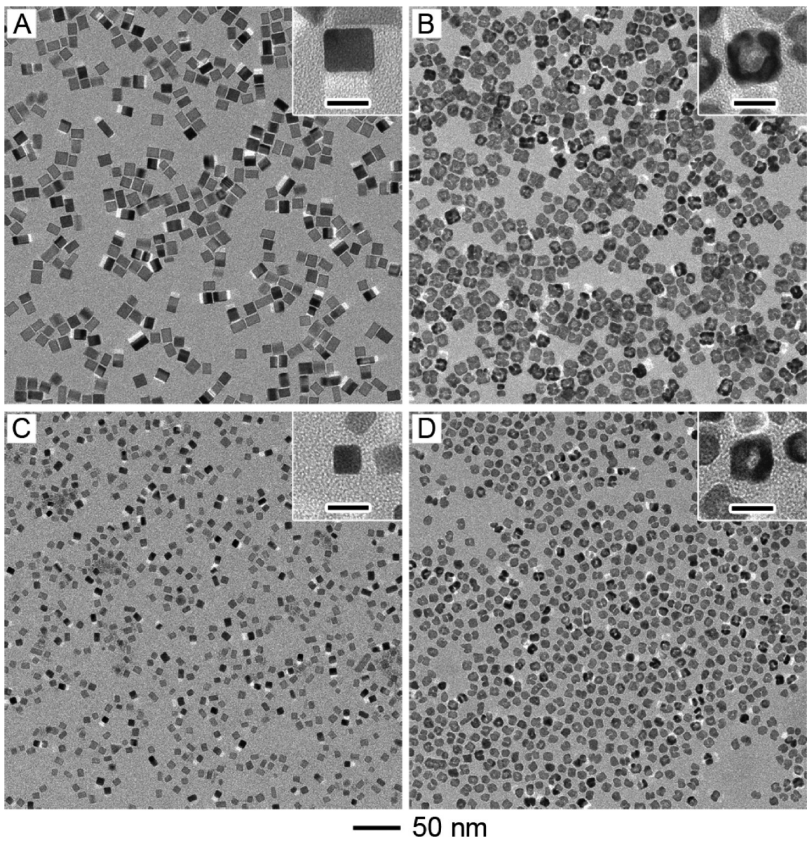

Figure 4. TEM images of (A, C) Pd nanocubes of 10 and 6 nm in size, respectively and (B, D) their corresponding Pd−Pt alloy nanocages synthesized using the standard procedure. The insets show the TEM image of individual nanocrystals at a higher magnification. The scale bars in the insets are 10 nm.

of Pd−Pt nanodendrites. In the absence of a reducing agent (e.g., CA, PVP, or AA, Figure S5C in the Supporting Information), only galvanic replacement between Pd nanocubes and $PtCl_4^{2-}$ ions occurred, and finally Pd−Pt concave nanocubes were formed. We can conclude that the use of a reducing agent with an appropriate reducing power played a critical role in the formation of Pd−Pt alloy nanocages. The amount of KBr in the solution was also found to be of great importance for the synthesis of Pd−Pt alloy nanocages because Br^- ions could promote the galvanic replacement reaction between Pd nanocrystals and $PtCl_4^{2-}$.[39] When no additional KBr was added, only Pd−Pt nanocrystals with a slight concave structure were generated due to oxidation and dissolution of Pd *via* galvanic replacement reaction with $PtCl_4^{2-}$ (Figure S5D in the Supporting Information). In this case, we believe that the small amount of Br^- adsorbed on the {100} side faces of Pd nanocubes during their synthesis was responsible for the galvanic replacement. Because of the slow galvanic replacement, most of the $PtCl_4^{2-}$ ions were reduced by CA to generate small Pt nanoparticles as marked by arrows in Figure S5D in the Supporting Information. In our previous report,[39] H_2PtCl_6 was employed as a Pt precursor to react with Pd nanocubes in the presence of Br^-, and Pd−Pt bimetallic concave nanocubes were obtained as final products. The reaction rate of galvanic replacement was found to be significantly reduced by replacing H_2PtCl_6 with K_2PtCl_4 due to the change in pH and oxidation state. Here we also investigated the effect of oxidation state on the formation of Pd−Pt alloy nanocages. Figure S6 in the Supporting Information shows the TEM image of a product obtained using the standard procedure except for the replacement of K_2PtCl_4 with H_2PtCl_6. As can be seen, the product only contained irregular aggregates of Pt nanoparticles with sizes ranging from 3 to 18 nm. We believe that the rapid galvanic replacement and slow reduction rate (due to the use of H_2PtCl_6, a precursor with a higher oxidation state) were responsible for the formation of the irregular aggregates of Pt nanoparticles.

The size of Pd−Pt alloy nanocages could be simply controlled by using Pd nanocubes with different sizes as the sacrificial templates. Figure 4 shows TEM images of Pd nanocubes of 10 and 6 nm in size, respectively, which were used as the sacrificial templates and their corresponding Pd−Pt nanocages. From the images, Pd nanocubes of 10 and 6 nm in size were both transformed into nanocages in high quality with slightly increased sizes due to a combination of galvanic replacement and overgrowth *via* coreduction. However, it was very difficult to control the morphology of the resultant Pd−Pt nanocages by varying the shape of the sacrificial templates. For example, when truncated octahedrons of Pd were employed as the sacrificial

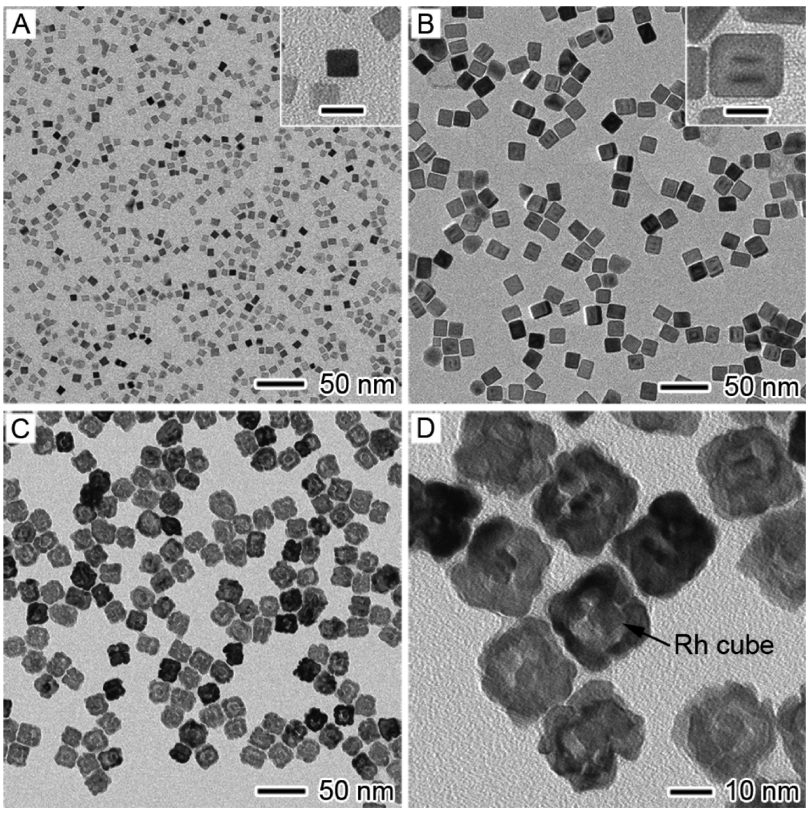

Figure 5. (A) TEM image of cubic Rh seeds of 6−7 nm in size. (B) TEM image of Rh@Pd core−shell nanocubes synthesized using seed-mediated overgrowth. (C, D) TEM images of Rh@Pd−Pt nanocages with a yolk-shell structure that were prepared using the standard procedure except for the use of Rh@Pd core−shell nanocubes as the templates. The scale bars in the insets are 10 nm.

templates, most of the Pd−Pt nanocrystals (Figure S7 in the Supporting Information) prepared using the standard procedure had an irregular shape with a concave structure on the surface, together with a few hollow nanostructures (marked by arrows). As revealed in our previous study,[39] the bromide-induced galvanic replacement reaction had a high selectivity toward the {100} facets of Pd. For truncated octahedrons, there was only a small portion of {100} facets. The rate for dissolution of Pd atoms from Pd{100} facets *via* galvanic replacement was relatively slow. In the meantime, the newly formed Pd^{2+} and remaining $PtCl_4^{2-}$ ions were both reduced by CA and then codeposited on the side faces of the templates to form an alloy structure, which could block the galvanic replacement reaction. As such, only irregular nanocrystals with a concave shape were obtained when truncated octahedrons of Pd were used as the sacrificial templates.

We also employed Rh@Pd core−shell nanocubes as the sacrificial templates for synthesis of Rh@Pd−Pt nanocages with a yolk-shell structure. The Rh@Pd core−shell nanocubes were synthesized by overgrowth in an aqueous solution containing KBr, PVP, AA, and Na_2PdCl_4 with Rh nanocubes of 6−7 nm in size (Figure 5A) serving as the seeds at 80 °C for 3 h. From the TEM image (Figure 5B), we observed a large number of core−shell nanocrystals of about 16 nm in size with a cubic shape. The magnified TEM image (inset of Figure 5B) clearly shows that there was a single Rh seed in the center of each core−shell nanocube. Obviously, epitaxial growth of a Pd shell occurred on the surface of each Rh core during the reaction. Starting with the Rh@Pd core−shell nanocubes, Rh@Pd−Pt yolk-shell nanocages (Figure 5C) were formed using the standard procedure through a combination of galvanic replacement and coreduction. Careful examination (Figure 5D) indicates that the hollow nanostructures essentially retained their original cubic shape with a slightly increased size, and most of them contained a Rh nanocube (marked by an arrow) in the center. We believed that this approach can be extended to synthesize other types of yolk-shell nanocages for various applications.

Figure 6 shows a plausible mechanism responsible for the formation of Pd−Pt nanocages, together with a brief account of the morphological evolution during a synthesis. As shown in our previous work,[39] Br^- ions could promote the galvanic replacement between Pd nanocubes and $PtCl_4^{2-}$ ions. Moreover, this galvanic replacement exhibited selectivity toward the {100} facets of Pd nanocrystals in the presence of Br^- ions. As such, the side faces of a Pd nanocube were slightly excavated in the very early stage due to the Br^--induced galvanic replacement, resulting in the formation of a concave structure (step 1). At the same time,

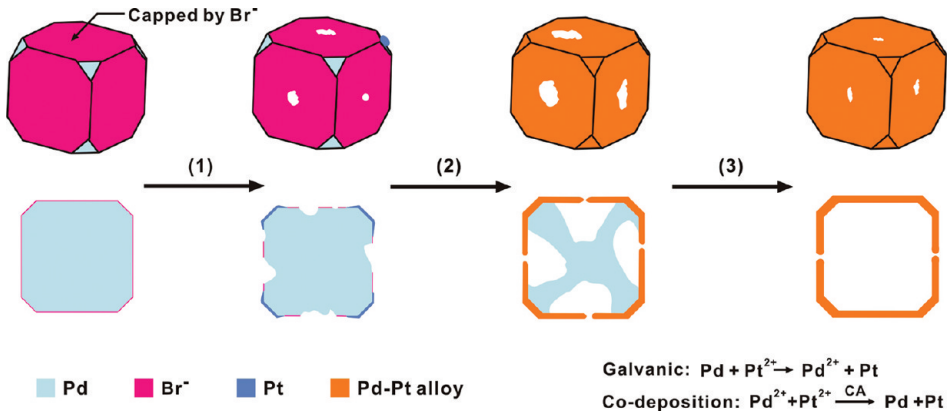

Figure 6. A schematic illustrating how the morphology and composition of the Pd–Pt alloy nanocage changed as a function of reaction time. Note that the reactivity of Pd atoms in the newly formed Pd–Pt alloy walls was lower relative to the Pd atoms in the original nanocube, and thus they had selectivity toward the galvanic replacement reaction with $PtCl_4^{2-}$.

coreduction of the $PdCl_4^{2-}$ (from the galvanic replacement) and remaining $PtCl_4^{2-}$ ions by CA would start to occur and accompany the galvanic replacement reaction during the entire synthesis. The newly formed Pd and Pt atoms were codeposited onto the side faces, starting from the concave regions between the corners, to generate an alloyed structure (step 2). As the reaction proceeded, the original Pd nanocube gradually disappeared due to the galvanic replacement. Meanwhile, side faces made of Pd–Pt alloys with exposed {100} facets were formed *via* codeposition owing to the stabilization of the {100} facets by selective adsorption of Br^- (step 3). It should be pointed out that the Pd atoms in the newly formed Pd–Pt alloy walls could not be oxidized back to ions through galvanic replacement due to their higher stability relative to the Pd atoms in the original nanocube. This difference in reactivity was critical to the formation of Pd–Pt alloy nanocages. There were also a number of small pores on the side faces of the nanocages, serving as channels for transportation of ions required for galvanic replacement. Finally, the Pd nanocube completely disappeared due to galvanic replacement, and a Pd–Pt alloy nanocage was formed *via* the coreduction process. It is clear that the rate of galvanic replacement between the Pd nanocubes and $PtCl_4^{2-}$ ions was of great importance for the formation of Pd–Pt alloy nanocages due to the need of a supply of Pd precursor for the subsequent codeposition process. As such, high concentrations of Br^- and $PtCl_4^{2-}$ ions, together with a high temperature, could speed up the galvanic replacement and thus facilitate the formation of Pd–Pt alloy nanocages. In addition, an appropriate reduction rate (i.e., choose of a proper reductant) was also indispensible for the formation of Pd–Pt alloy nanocages.

The Pd–Pt alloy nanocages with average edge lengths of 20, 12, and 8 nm, respectively, were evaluated as catalysts for the PROX reaction using H_2 feeds contaminated with 1% CO (by vol) and 0.5% O_2 (by vol). We benchmarked the catalytic activity of these nanocages against the commercial Pt/C catalyst (E-TEK, 20 wt % of 3.2 nm Pt nanoparticles on Vulcan XC-72 carbon support) and Pd cubes of 18 nm in size. For all samples, the total loading of metals was 1 mg (100 mg of catalyst, 1 wt % of metal). The temperature-programmed reaction (TPR) data for the PROX over the different catalysts are shown in Figure 7. The catalysts based on Pd nanocubes and Pt/C only showed maximum CO conversion of about 32% and 65% (Figure 7A) under 250 °C, respectively, which were significantly lower than those of all the different Pd–Pt alloy nanocages. In addition, the onset temperatures for these two reference catalysts were much higher than those of the Pd–Pt nanocages. For all the catalysts, the CO selectivity decreased with increasing temperature (Figure 7B). It dropped from 100% to 90% for the Pd–Pt alloy nanocages and from 81% to 74% for the Pt/C in the low temperature range of 90–150 °C. Overall, the Pd nanocubes showed the lowest CO selectivity, which decreased from 60% to 48% in the same low temperature range. As a result, the Pd–Pt nanocages with different sizes are much more active and selective for CO oxidation in excess hydrogen than both the Pd nanocubes and Pt/C.

We believe that the addition of Pd as a component of the Pd–Pt alloy nanocages together with the formation of hollow/porous structures are responsible for the enhanced activity and selectivity for the PROX reaction. It is well-known that monometallic catalysts, such as Pd or Pt particles, usually show poor activity for the PROX reaction.[41,42] Taking the Pt catalyst as an example, the maximum CO conversion in a hydrogen-rich mixture was only observed at over 300 °C with a relatively poor selectivity <50%.[42] Studies by many groups indicate that the catalytic activity of a Pd (or Pt) catalyst could be increased by incorporating Pt (or Pd) into the catalyst, in the form of a Pt–Pd alloy. Thus far, this approach has been proven to be an attractive strategy for enhancing the catalytic properties including activity and selectivity.[43]

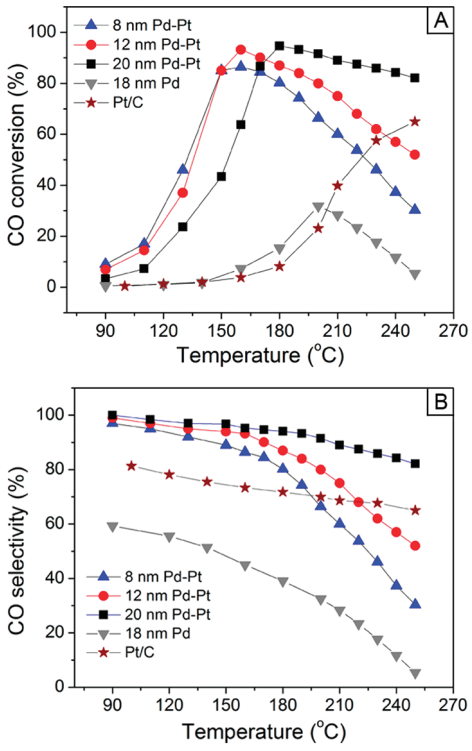

Figure 7. Plots of (A) activity and (B) selectivity as a function of reaction temperature for CO preferential oxidation in the presence of hydrogen on Pd–Pt alloy nanocages of 8, 12, and 20 nm in size, Pd nanocubes of 18 nm in size, and the commercial Pt/C catalyst.

The size of Pd–Pt nanocages was also found to have an impact on their catalytic performance. Specifically, reducing the size of the Pd–Pt nanocages increased the conversion rate of CO (Figure 7A). The maximum conversion temperature also strongly depended on the size of the nanocages. For example, for the 8 nm Pd–Pt nanocages, the maximum conversion temperature was 150 °C, much lower than those of the larger nanocages. The enhanced activity with decreasing the size of the Pd–Pt nanocages can be attributed to the higher specific surface area and thinner wall thicknesses. However, the selectivity of CO oxidation over the Pd–Pt nanocages with smaller size decreased much more dramatically with increasing the temperature (Figure 7B). In this case, the larger hollow interiors in the Pd–Pt nanocages might be responsible for the higher selectivity by buffering the oxidation of H_2.

CONCLUSIONS

We have demonstrated the synthesis of Pd–Pt alloy nanocages with hollow interiors and porous walls using Pd nanocubes with different sizes as the sacrificial templates. The Pd nanocubes were initially excavated from the side faces due to the galvanic replacement, and then Pd and Pt atoms were deposited on the side faces in the form of an alloy due to coreduction of the $PdCl_4^{2-}$ and $PtCl_4^{2-}$ ions by CA. The morphology of the final product depended on a number of parameters, including the presence of Br^- ions, the type of reducing agent, the amount of added $PtCl_4^{2-}$, and the temperature. This work provides a facile approach to the production of Pd–Pt alloy nanocages with improved performance for PROX, a reaction critical to the commercialization of PCMFCs. Specifically, the Pd–Pt alloy nanocages exhibited enhanced activity and selectivity for the PROX reaction relative to both Pd nanocubes and the commercial Pt/C due to the alloy composition and hollow structures. The Pd–Pt nanocages with smaller sizes were found to exhibit higher CO conversation rates and lower maximum conversion temperatures due to their higher specific surface areas, albeit they had lower selectivity for the PROX reaction because of the smaller hollow interiors.

EXPERIMENTAL SECTION

Chemicals and Materials. Sodium tetrachloropalladate(II) (Na_2PdCl_4, Sigma-Aldrich, 99.998%), potassium tetrachloroplatinate(II) (K_2PtCl_4, Sigma-Aldrich, 99.99%), sodium hexachlororhodate(III) (Na_3RhCl_6, Sigma-Aldrich), potassium bromide (KBr, Fisher Scientific), potassium chloride (KCl, J. T. Baker), poly(vinyl pyrrolidone) (PVP, MW ≈ 55 000, Sigma-Aldrich), citric acid (CA, Fisher Scientific), L-ascorbic acid (AA, Sigma-Aldrich), ethylene glycol (EG, J. T. Baker), and ethanol (Pharmco Products, 200 proof) were all used as received. All aqueous solutions were prepared using deionized water with a resistivity of 18.2 MΩ cm.

Synthesis of Pd Nanocubes. The Pd nanocubes were synthesized by adding a Na_2PdCl_4 solution into a mixture of AA, KBr, and KCl according to our previous report.[44] In a typical synthesis, 8.0 mL of an aqueous solution containing 105 mg of PVP, 60 mg of AA, and different amounts of KBr and KCl was placed in a vial and preheated to 80 °C in an oil bath under magnetic stirring for 10 min. Subsequently, 3.0 mL of an aqueous solution containing 57 mg of Na_2PdCl_4 was added with a pipet. After the vial had been capped, the reaction was allowed to continue at 80 °C for 3 h. The size of Pd nanocubes was controlled by varying the amounts of KBr and KCl: for example, Pd nanocubes of 18, 10, and 6 nm in edge length were obtained with the use of 600 mg of KBr, 300 mg of KBr, and a mixture of 5 mg of KBr and 185 mg of KCl, respectively. The product was collected by centrifugation, washed three times with water to remove excess PVP, and redispersed in 11 mL of water.

Synthesis of Cubic Rh Seeds of 6–7 nm in Size. The Rh nanocubes were prepared by adding a Na_3RhCl_6 solution into a mixture containing AA, KBr, PVP, and EG (serving as the solvent), according to our previous report.[45] In a typical synthesis, 52.8 mg of AA, 108 mg of KBr, and 133 mg of PVP were dissolved in 13 mL of EG hosted in a three-neck flask. The flask was then equipped with a reflux condenser and a Teflon-coated magnetic stir bar, preheated in air at 110 °C for 2 h, and then ramped to 140 °C. Meanwhile, 46.2 mg of Na_3RhCl_6 was dissolved in 6 mL of EG at room temperature. This solution was then injected into the flask through a syringe pump at a rate of 60 mL/h for the first 1.1 and 4 mL/h for the remaining 4.9 mL of the precursor solution. After the reaction had proceeded for 3 h, the reaction mixture was cooled down naturally. The product was dialyzed seven times to completely remove EG and KBr, followed by redispersion in 19 mL of water.

Synthesis of Rh–Pd Core–Shell Nanocubes. The Rh@Pd core–shell nanocubes were prepared using a seed-mediated method. In a typical synthesis, 8.0 mL of an aqueous solution containing 105 mg of PVP, 60 mg of AA, 400 mg of KBr, and 1 mL of the suspension of cubic Rh seeds was placed in a vial and heated to 80 °C in an oil bath under magnetic stirring for 10 min. Subsequently, 3.0 mL of an aqueous solution containing 10 mg of Na_2PdCl_4 was added with a pipet. After the vial had been capped, the reaction was allowed to continue at 80 °C for 3 h. The product was collected by centrifugation, washed three times with water to remove excess PVP, and redispersed in 11 mL of water.

Synthesis of Pd–Pt Alloy Nanocages. In a standard procedure, 1 mL of the aqueous suspension of Pd nanocubes (18 nm in size) and 7 mL of an aqueous solution containing 33.3 mg of PVP, 300 mg of KBr, and 300 mg of CA were mixed in a glass vial. The mixture was heated to 90 °C in air under magnetic stirring. Meanwhile, 28 mg of K_2PtCl_4 was dissolved in 3 mL of deionized water. This aqueous solution was then injected into the solution containing PVP, KBr, and Pd nanocubes using a syringe pump at a rate of 1 mL/min. The reaction mixture was then heated to 90 °C for 12 h in air. Finally, the solution was centrifuged and washed three times with water to remove PVP before characterization. We systematically investigated the effects of a number of parameters, including the amount of K_2PtCl_4, the duration of reaction, the size of Pd nanocubes, the temperature, as well as the type of reducing agent on the final morphology of resultant Pd–Pt alloy nanocages.

Morphological, Structural, and Elemental Characterizations. Transmission electron microscopy (TEM) images were taken using a Tecnai G2 Spirit Twin microscope (FEI, Hillsboro, OR) operated at 120 kV. HRTEM, HAADF-STEM, and EDX analyses were performed using a JEOL 2100F microscope (JEOL, Tokyo, Japan) operated at 200 kV. SEM images were captured using a Nova NanoSEM 230 field-emission microscope (FEI, Hillsboro, OR) operated at 30 kV. The percentages of Pd and Pt in the samples were determined using ICP-MS (Perkin-Elmer Elan DRC II).

PROX Reaction. In order to exclude the influence of support on the catalytic activity, we selected ZnO nanowires as the support, which were synthesized *via* a thermal evaporation method.[46] The preparation of a Pd–Pt/ZnO catalyst involved three steps: (i) the as-synthesized ZnO nanowires were dispersed in ethanol by sonication; (ii) the as-prepared Pd–Pt nanocages were added into the solution under intensive magnetic stirring; and (iii) the Pd–Pt/ZnO catalyst was collected by filtration, washed with ethanol, and kept in an oven overnight at 100 °C. The activities of different Pd–Pt/ZnO catalysts toward PROX were evaluated in a homemade, fixed-bed quartz tubular reactor. After the Pd–Pt/ZnO catalyst (100 mg, 1 wt % of Pd and Pt) had been placed in the reactor, the reactant gases (1.0% CO, 0.5% O_2, and H_2 balance) were flown through the reactor at a rate of 60 mL/min. The compositions of the reaction product exiting the reactor were monitored by gas chromatography. For comparison, Pd nanocubes and commercial Pt/C were also tested as catalysts for the PROX reaction.

Acknowledgment. This work was supported in part by a DOE subcontract from the University of Delaware (Grant DE-FG02-03 ER15468) and startup funds from Washington University in St. Louis. As a visiting scholar from Zhejiang University, H.Z. was also partially supported by the "New Star Program" of Zhejiang University. As a visiting student from Xiamen University, M.J. was also partially supported by the China Scholarship Council. J. W. was supported by a grant from CNMT (Grant 2010K000336) under the 21st Frontier R&D Program of the MEST, Korea. Part of the research was performed at the Nano Research Facility, a member of the National Nanotechnology Infrastructure Network (NNIN), which is supported by the NSF under Award ECS-0335765.

Supporting Information Available: TEM images of Pd nanocubes, TEM images of Pd–Pt nanocages prepared using different combinations of parameters including the use of 70 mg K_2PtCl_4 as a precursor, truncated Pd octahedrons as templates, different temperatures, PVP as a reducing agent, AA as a reducing agent, the absence of reducing agent, and the absence of KBr, and EDX spectra of the Pd–Pt nanocages. This material is available free of charge *via* the Internet at http://pubs.acs.org.

REFERENCES AND NOTES

1. Steele, B. C. H.; Heinzel, A. Materials for Fuel-Cell Technologies. *Nature* **2001**, *414*, 345–352.
2. Arico, A. S.; Bruce, P.; Scrosati, B.; Tarascon, J. M.; Van Schalkwijk, W. Nanostructured Materials for Advanced Energy Conversion and Storage Devices. *Nat. Mater.* **2005**, *4*, 366–377.
3. Genorio, B.; Strmcnik, D.; Subbaraman, R.; Tripkovic, D.; Karapetrov, G.; Stamenkovic, V. R.; Pejovnik, S.; Markovic, N. M. Selective Catalysts for the Hydrogen Oxidation and Oxygen Reduction Reactions by Patterning of Platinum with Calix[4]arene Molecules. *Nat. Mater.* **2010**, *9*, 998–1003.
4. Brandon, N. P.; Skinner, S.; Steele, B. C. H. Recent Advances in Materials for Fuel Cells. *Annu. Rev. Mater. Res.* **2003**, *33*, 183–213.
5. Shao, Y. Y.; Liu, J.; Wang, Y.; Lin, Y. H. Novel Catalyst Support Materials for PEM Fuel Cells: Current Status and Future Prospects. *J. Mater. Chem.* **2009**, *19*, 46–59.
6. Lim, B.; Jiang, M. J.; Camargo, P. H. C.; Cho, E. C.; Tao, J.; Lu, X. M.; Zhu, Y. M.; Xia, Y. Pd-Pt Bimetallic Nanodendrites with High Activity for Oxygen Reduction. *Science* **2009**, *324*, 1302–1305.
7. Strmcnik, D.; Kodama, K.; van der Vliet, D.; Greeley, J.; Stamenkovic, V. R.; Markovic, N. M. The Role of Non-covalent Interactions in Electrocatalytic Fuel-Cell Reactions on Platinum. *Nat. Chem.* **2009**, *1*, 466–472.
8. Stamenkovic, V. R.; Mun, B. S.; Arenz, M.; Mayrhofer, K. J. J.; Lucas, C. A.; Wang, G. F.; Ross, P. N.; Markovic, N. M. Trends in Electrocatalysis on Extended and Nanoscale Pt-Bimetallic Alloy Surfaces. *Nat. Mater.* **2007**, *6*, 241–247.
9. Peng, Z. M.; Yang, H. Designer Platinum Nanoparticles: Control of Shape, Composition in Alloy, Nanostructure and Electrocatalytic Property. *Nano Today* **2009**, *4*, 143–164.
10. Li, Y. M.; Somorjai, G. A. Nanoscale Advances in Catalysis and Energy Applications. *Nano Lett.* **2010**, *10*, 2289–2295.
11. Montano, M.; Bratlie, K.; Salmeron, M.; Somorjai, G. A. Hydrogen and Deuterium Exchange on Pt(111) and Its Poisoning by Carbon Monoxide Studied by Surface Sensitive High-Pressure Techniques. *J. Am. Chem. Soc.* **2006**, *128*, 13229–13234.
12. Kim, G.; Jhi, S. H. Carbon Monoxide-Tolerant Platinum Nanoparticle Catalysts on Defect-Engineered Graphene. *ACS Nano* **2011**, *5*, 805–810.
13. Kucernak, A. R.; Offer, G. J. The Role of Adsorbed Hydroxyl Species in the Electrocatalytic Carbon Monoxide Oxidation Reaction on Platinum. *Phys. Chem. Chem. Phys.* **2008**, *10*, 3699–3711.
14. Uchida, H.; Izumi, K.; Aoki, K.; Watanabe, M. Temperature-Dependence of Hydrogen Oxidation Reaction Rates and CO-Tolerance at Carbon-Supported Pt, Pt-Co, and Pt-Ru Catalysts. *Phys. Chem. Chem. Phys.* **2009**, *11*, 1771–1779.
15. Park, E. D.; Lee, D.; Lee, H. C. Recent Progress in Selective CO Removal in a H_2-Rich Stream. *Catal. Today* **2009**, *139*, 280–290.
16. Bion, N.; Epron, F.; Moreno, M.; Marino, F.; Duprez, D. Preferential Oxidation of Carbon Monoxide in the Presence of Hydrogen (PROX) over Noble Metals and Transition Metal Oxides: Advantages and Drawbacks. *Top. Catal.* **2008**, *51*, 76–88.
17. Ouyang, X.; Bednarova, L.; Besser, R. S.; Ho, P. Preferential Oxidation (PROX) in a Thin-Film Catalytic Microreactor: Advantages and Limitations. *AIChE J.* **2005**, *51*, 1758–1772.
18. Alayoglu, S.; Nilekar, A. U.; Mavrikakis, M.; Eichhorn, B. Ru-Pt Core-Shell Nanoparticles for Preferential Oxidation of Carbon Monoxide in Hydrogen. *Nat. Mater.* **2008**, *7*, 333–338.
19. Alayoglu, S.; Eichhorn, B. Rh-Pt Bimetallic Catalysts: Synthesis, Characterization, and Catalysis of Core-Shell, Alloy, and Monometallic Nanoparticles. *J. Am. Chem. Soc.* **2008**, *130*, 17479–17486.

20. Huang, S. J.; Hara, K.; Fukuoka, A. Green Catalysis for Selective CO Oxidation in Hydrogen for Fuel Cell. *Energy Environ. Sci.* **2009**, *2*, 1060–1068.
21. Nilekar, A. U.; Alayoglu, S.; Eichhorn, B.; Mavrikakis, M. Preferential CO Oxidation in Hydrogen: Reactivity of Core-Shell Nanoparticles. *J. Am. Chem. Soc.* **2010**, *132*, 7418–7428.
22. Lee, Y. W.; Ko, A. R.; Han, S. B.; Kim, H. S.; Park, K. W. Synthesis of Octahedral Pt-Pd Alloy Nanoparticles for Improved Catalytic Activity and Stability in Methanol Electrooxidation. *Phys. Chem. Chem. Phys.* **2011**, *13*, 5569–5572.
23. Lee, H. J.; Habas, S. E.; Somorjai, G. A.; Yang, P. D. Localized Pd Overgrowth on Cubic Pt Nanocrystals for Enhanced Electrocatalytic Oxidation of Formic Acid. *J. Am. Chem. Soc.* **2008**, *130*, 5406–5407.
24. Peng, Z. M.; Yang, H. Synthesis and Oxygen Reduction Electrocatalytic Property of Pt-on-Pd Bimetallic Heteronanostructures. *J. Am. Chem. Soc.* **2009**, *131*, 7542–7543.
25. Lim, B.; Wang, J. G.; Camargo, P. H. C.; Cobley, C. M.; Kim, M. J.; Xia, Y. Twin-Induced Growth of Palladium-Platinum Alloy Nanocrystals. *Angew. Chem., Int. Ed.* **2009**, *48*, 6304–6308.
26. Yin, A. X.; Min, X. Q.; Zhang, Y. W.; Yan, C. H. Shape-Selective Synthesis and Facet-Dependent Enhanced Electrocatalytic Activity and Durability of Monodisperse Sub-10 nm Pt-Pd Tetrahedrons and Cubes. *J. Am. Chem. Soc.* **2011**, *133*, 3816–3819.
27. Habas, S. E.; Lee, H.; Radmilovic, V.; Somorjai, G. A.; Yang, P. Shaping Binary Metal Nanocrystals through Epitaxial Seeded Growth. *Nat. Mater.* **2007**, *6*, 692–697.
28. Huang, X. Q.; Zhang, H. H.; Guo, C. Y.; Zhou, Z. Y.; Zheng, N. F. Simplifying the Creation of Hollow Metallic Nanostructures: One-Pot Synthesis of Hollow Palladium/Platinum Single-Crystalline Nanocubes. *Angew. Chem., Int. Ed.* **2009**, *48*, 4808–4812.
29. Chen, Z. W.; Waje, M.; Li, W. Z.; Yan, Y. S. Supportless Pt and PtPd Nanotubes as Electrocatalysts for Oxygen-Reduction Reactions. *Angew. Chem., Int. Ed.* **2007**, *46*, 4060–4063.
30. Mahmoud, M. A.; Saira, F.; El-Sayed, M. A. Experimental Evidence for the Nanocage Effect in Catalysis with Hollow Nanoparticles. *Nano Lett.* **2010**, *10*, 3764–3769.
31. Wang, L.; Yamauchi, Y. Autoprogrammed Synthesis of Triple-Layered Au@Pd@Pt Core-Shell Nanoparticles Consisting of a Au@Pd Bimetallic Core and Nanoporous Pt Shell. *J. Am. Chem. Soc.* **2010**, *132*, 13636–13638.
32. Shao, M. H.; Shoemaker, K.; Peles, A.; Kaneko, K.; Protsailo, L. Pt Monolayer on Porous Pd-Cu Alloys as Oxygen Reduction Electrocatalysts. *J. Am. Chem. Soc.* **2010**, *132*, 9253–9255.
33. Zeng, H. C. Synthesis and Self-Assembly of Complex Hollow Materials. *J. Mater. Chem.* **2011**, *21*, 7511–7526.
34. Wang, Y.; Angelatos, A. S.; Caruso, F. Template Synthesis of Nanostructured Materials *via* Layer-by-Layer Assembly. *Chem. Mater.* **2008**, *20*, 848–858.
35. Alia, S. M.; Zhang, G.; Kisailus, D.; Li, D. S.; Gu, S.; Jensen, K.; Yan, Y. S. Porous Platinum Nanotubes for Oxygen Reduction and Methanol Oxidation Reactions. *Adv. Funct. Mater.* **2010**, *20*, 3742–3746.
36. Kijima, T.; Yoshimura, T.; Uota, M.; Ikeda, T.; Fujikawa, D.; Mouri, S.; Uoyama, S. Noble-Metal Nanotubes (Pt, Pd, Ag) from Lyotropic Mixed-Surfactant Liquid-Crystal Templates. *Angew. Chem., Int. Ed.* **2004**, *43*, 228–232.
37. Skrabalak, S. E.; Chen, J. Y.; Sun, Y. G.; Lu, X. M.; Au, L.; Cobley, C. M.; Xia, Y. Gold Nanocages: Synthesis, Properties, and Applications. *Acc. Chem. Res.* **2008**, *41*, 1587–1595.
38. Sun, Y. G.; Mayers, B.; Xia, Y. Metal Nanostructures with Hollow Interiors. *Adv. Mater.* **2003**, *15*, 641–646.
39. Zhang, H.; Jin, M. S.; Wang, J. G.; Li, W. Y.; Camargo, P. H. C.; Kim, M. J.; Yang, D. R.; Xie, Z. X.; Xia, Y. Synthesis of Pd-Pt Bimetallic Nanocrystals with a Concave Structure through a Bromide-Induced Galvanic Replacement Reaction. *J. Am. Chem. Soc.* **2011**, *133*, 6078–6089.
40. Washio, I.; Xiong, Y. J.; Yin, Y. D.; Xia, Y. Reduction by the End Groups of Poly(vinyl pyrrolidone): A New and Versatile Route to the Kinetically Controlled Synthesis of Ag Triangular Nanoplates. *Adv. Mater.* **2006**, *18*, 1745–1749.
41. Bera, P.; Gayen, A.; Hegde, M.; Lalla, N.; Spadaro, L.; Frusteri, F.; Arena, F. Promoting Effect of CeO_2 in Combustion Synthesized Pt/CeO_2 Catalyst for CO Oxidation. *J. Phys. Chem. B* **2003**, *107*, 6122–6130.
42. Kim, D.; Lim, M. Kinetics of Selective CO Oxidation in Hydrogen-Rich Mixtures on Pt/Alumina Catalysts. *Appl. Catal., A* **2002**, *224*, 27–38.
43. Parinyaswan, A.; Pongstabodee, S.; Luengnaruemitchai, A. Catalytic Performances of Pt-Pd/CeO_2 Catalysts for Selective CO Oxidation. *Int. J. Hydrogen Energy* **2006**, *31*, 1942–1949.
44. Jin, M. S.; Liu, H. Y.; Zhang, H.; Xie, Z. X.; Liu, J. Y.; Xia, Y. Synthesis of Pd Nanocrystals Enclosed by {100} Facets and with Sizes <10 nm for Application in CO Oxidation. *Nano Res.* **2011**, *4*, 83–91.
45. Zhang, H.; Li, W. Y.; Jin, M. S.; Zeng, J. E.; Yu, T. K.; Yang, D. R.; Xia, Y. Controlling the Morphology of Rhodium Nanocrystals by Manipulating the Growth Kinetics with a Syringe Pump. *Nano Lett.* **2011**, *11*, 898–903.
46. Pan, Z. W.; Dai, Z. R.; Wang, Z. L. Nanobelts of Semiconducting Oxides. *Science* **2001**, *291*, 1947–1949.